JOURNAL OF SYNCHROTRON RADIATION

ISSN 1600-5775

# Advancements towards the implementation of clinical phase-contrast breast computed tomography at Elettra

Renata Longo,[a,b] Fulvia Arfelli,[a,b] Deborah Bonazza,[c] Ubaldo Bottigli,[d,e] Luca Brombal,[a,b]* Adriano Contillo,[f,g] Maria A. Cova,[c] Pasquale Delogu,[d,e] Francesca Di Lillo,[h,i] Vittorio Di Trapani,[d,e] Sandro Donato,[a,b] Diego Dreossi,[j] Viviana Fanti,[k,l] Christian Fedon,[m,b] Bruno Golosio,[k,l] Giovanni Mettivier,[h,i] Piernicola Oliva,[n,l] Serena Pacilè,[j,o] Antonio Sarno,[h,i] Luigi Rigon,[a,b] Paolo Russo,[h,i] Angelo Taibi,[f,g] Maura Tonutti,[p] Fabrizio Zanconati[c] and Giuliana Tromba[j]

[a]Department of Physics, University of Trieste, 34127 Trieste, Italy, [b]INFN Division of Trieste, 34127 Trieste, Italy, [c]Department of Medical Science, Cattinara Hospital, University of Trieste, 34149 Trieste, Italy, [d]Department of Physical Sciences, Earth and Environment, University of Siena, 53100 Siena, Italy, [e]INFN Division of Pisa, 34127 Pisa, Italy, [f]Department of Physics and Earth Science, University of Ferrara, 44122 Ferrara, Italy, [g]INFN Division of Ferrara, 44122 Ferrara, Italy, [h]Department of Physics 'E. Pancini', University of Napoli 'Federico II', 80126 Napoli, Italy, [i]INFN Division of Napoli, 80126 Napoli, Italy, [j]Elettra-Sincrotrone Trieste SCpA, 34149 Trieste, Italy, [k]Department of Physics, University of Cagliari, 09042 Monserrato (CA), Italy, [l]INFN Division of Cagliari, 09042 Monserrato (CA), Italy, [m]Department of Radiology and Nuclear Medicine, Radboudumc, Nijmegen, The Netherlands, [n]Department of Chemistry and Pharmacy, University of Sassari, 07100 Sassari, Italy, [o]Department of Engineering and Architecture, University of Trieste, 34127 Trieste, Italy, and [p]ASUITS, Trieste University Hospital, Department of Radiology, 34100 Trieste, Italy.
*Correspondence e-mail: luca.brombal@ts.infn.it

Received 17 December 2018
Accepted 23 April 2019

Edited by A. Momose, Tohoku University, Japan

**Keywords:** breast CT; phase contrast; free space propagation; single photon counting.

**Supporting information**: this article has supporting information at journals.iucr.org/s

Breast computed tomography (BCT) is an emerging application of X-ray tomography in radiological practice. A few clinical prototypes are under evaluation in hospitals and new systems are under development aiming at improving spatial and contrast resolution and reducing delivered dose. At the same time, synchrotron-radiation phase-contrast mammography has been demonstrated to offer substantial advantages when compared with conventional mammography. At Elettra, the Italian synchrotron radiation facility, a clinical program of phase-contrast BCT based on the free-space propagation approach is under development. In this paper, full-volume breast samples imaged with a beam energy of 32 keV delivering a mean glandular dose of 5 mGy are presented. The whole acquisition setup mimics a clinical study in order to evaluate its feasibility in terms of acquisition time and image quality. Acquisitions are performed using a high-resolution CdTe photon-counting detector and the projection data are processed via a phase-retrieval algorithm. Tomographic reconstructions are compared with conventional mammographic images acquired prior to surgery and with histologic examinations. Results indicate that BCT with monochromatic beam and free-space propagation phase-contrast imaging provide relevant three-dimensional insights of breast morphology at clinically acceptable doses and scan times.

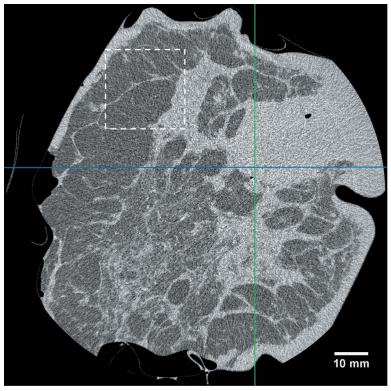




## 1. Introduction

Breast computed tomography (BCT) is a specific application of X-ray tomography. Even though the first clinical studies in BCT were published ten years ago (Lindfors *et al.*, 2008), this technique is not yet established in the radiological community. Only two BCT scanners are available on the market (O'Connell *et al.*, 2010; Koning, 2018; Kalender *et al.*, 2017; Berger *et al.*, 2019; AB-CT, 2019), but their use is not widespread and their role in the diagnostic process is still not well recognized (O'Connell *et al.*, 2014; Wienbeck *et al.*, 2017).

The first generation of BCT scanners is based on cone beam geometry (Sarno *et al.*, 2015) and, while keeping the acquisi-

tion time quite short, it suffers from contrast reduction due to scattered radiation (Sechopoulos, 2012). In order to overcome such limitation, a new generation of BCT systems, based on fan beam and photon-counting detectors, has been developed (Kalender *et al.*, 2012, 2017; Longo *et al.*, 2016). The fan beam setup adds complexity to the system requiring a spiral-CT acquisition and potentially longer scan times, suggesting the usefulness of a breast immobilizer system (Rößler *et al.*, 2015).

In addition to conventional X-ray imaging relying uniquely on the absorption properties of the sample, phase contrast (PhC) imaging techniques have been demonstrated to be suitable for improving the visibility of low-contrast features in soft tissues (Rigon, 2014). PhC imaging of the breast was investigated by a number of research teams (Coan *et al.*, 2013; Longo, 2016) and the free-space propagation technique has been exploited in two clinical mammography studies, the first based on conventional X-ray tubes (Tanaka *et al.*, 2005) and the second based on synchrotron radiation (Castelli *et al.*, 2011). In the first case, after a clinical trial encompassing 3835 examinations, no statistically significant difference was found in recall rates and cancer detection rates when compared with conventional film-screening mammography (Morita *et al.*, 2008). On the other hand, the synchrotron-radiation-based mammography trial demonstrated better image quality (Longo *et al.*, 2014), lower dose and higher diagnostic power with respect to digital mammography (Fedon *et al.*, 2018).

In this context, a phase-contrast breast computed tomography (PBCT) system is under development at Elettra, the Italian synchrotron radiation facility (Longo *et al.*, 2016; Sarno *et al.*, 2016; Delogu *et al.*, 2017*a*; Brombal *et al.*, 2019). The present setup is an upgrade of the PhC synchrotron radiation mammographic facility (Castelli *et al.*, 2011) and, as in the previous study, it is based on the free-space propagation modality. This technique is the simplest to implement among the phase-sensitive approaches since, having a sufficiently coherent source, it only requires to increase the object-to-detector distance with respect to the conventional absorption configuration. In this way, the collected image will show an enhanced edge contrast (*i.e.* edge enhancement) due to the interference of the refracted X-rays, resulting in an increased visibility of the interfaces between different structures, whose contrast is proportional to the Laplacian of the induced phase shift. An important difference between PhC mammography and PBCT is that, in the latter, a phase-retrieval procedure is applied to the projections prior to CT reconstruction (Cloetens *et al.*, 1996). In this work, the well known Paganin's single-shot retrieval algorithm is used (Paganin *et al.*, 2002): a brilliant discussion on the effects of phase retrieval on images acquired in free-space configuration has recently been published by Gureyev and co-authors (Gureyev *et al.*, 2017).

In the present paper, the latest results in the field of PBCT in the framework of the SYRMA-CT/SYRMA-3D collaboration are presented. In preliminary studies (Longo *et al.*, 2016; Sarno *et al.*, 2016) a prototype of a large-area high-efficiency photon-counting detector (Pixirad-8) was used (Bellazzini *et al.*, 2013; Vincenzi *et al.*, 2015) and the CT data were collected in a step-and-shoot mode, *i.e.* alternating rotation and projection acquisition. In this configuration a good image quality was achieved, also for large samples, even with a small number (*i.e.* a few hundreds) of projections thanks to iterative reconstruction techniques (Longo *et al.*, 2016; Delogu *et al.*, 2017*a*). Moving towards the clinical implementation, which requires an as-short-as-possible imaging time and an acceptable patient comfort, a continuous rotation during the CT scan is required. In this condition, a small number of projections means a large rotation angle spanned by the sample during each projection acquisition, which causes artifacts in the reconstructed images (Delogu *et al.*, 2017*a*). Currently, the optimization of the number of projections is still in progress (Donato *et al.*, 2019). In this work, images are acquired in continuous rotation with a large number of projections (*i.e.* 1200) and reconstructed via a standard filtered back projection (FBP) after the application of the phase-retrieval algorithm.

Especially when dealing with soft tissues, the trade-off between the recorded statistics and image contrast is critical in order to optimize the X-ray beam energy. Following the idea of Mittone and co-workers (Mittone *et al.*, 2014), the recorded statistics at a given dose, viz. the transmission over dose ratio, is the quantity to be optimized, thus high-energy beam should be preferred. For this reason, most of the scans published in our previous works were collected at the highest beam energy available at the beamline (38–40 keV). However, a recent paper by Baran and co-workers (Baran *et al.*, 2017) demonstrated that, at similar radiation dose levels, radiologists tend to prefer lower energies (32 keV) where, despite having a higher statistical noise due to the lower transmission through the sample, the soft tissue contrast is higher. In this framework, a simulation study developed by our collaboration (unpublished data) confirmed that, when the contrast-to-noise ratio (CNR) is optimized, the optimal energy for breast specimens with diameters of the order of 10 cm is in the range suggested by Baran *et al.* or lower. Conforming to these results, the beam energy (32 keV) used in this work is lower with respect to preliminary studies.

The activity of the SYRMA-CT/SYRMA-3D collaboration includes all the topics necessary for the implementation of a clinical study, ranging from an *ad hoc* Monte Carlo simulation software for dose evaluation (Fedon *et al.*, 2015; Mettivier *et al.*, 2016) to the development of a dedicated image quality assessment procedure (Contillo *et al.*, 2018). In this study, along with a thorough description of the experimental setup, we present the full scans of three mastectomy samples acquired with an upgraded version of Pixirad-8 detector encompassing a faster readout and a dedicated data pre-processing procedure (Brombal *et al.*, 2018*a*). The reconstructed CT volumes are compared with clinical X-ray investigations (*i.e.* mammography) acquired before surgery and with histological images. In addition, considerations on the usefulness of phase-retrieval procedure are reported and foreseeable major improvements in image quality due to larger propagation distances and dedicated iterative reconstruction algorithms are discussed.

## 2. Materials and methods

### 2.1. Beamline and acquisition setup

The tomographic images were acquired at the SYRMEP beamline at Elettra (Tromba *et al.*, 2010). The X-ray beam is produced by one storage ring bending magnet and the energy can be selected in the range 8.5–40 keV by means of a Si(111) double-crystal monochromator, providing an energy resolution of 0.1%. At the sample position the beam cross section is 220 mm (horizontal) × 3.5 mm (vertical, Gaussian shape, FWHM). The surgical specimens were imaged in a pendant geometry hanging from the patient support, constituted by a rotating table with an ergonomically designed aperture at the rotation center (Sarno *et al.*, 2016). Images were collected at the largest propagation distance presently available (1.6 m), that enables to detect phase-contrast effects and, along with the laminar shape of the beam, to avoid scattering contribution, thus not requiring anti-scattering grids or dedicated processing algorithms. A custom dosimetric system, previously developed for the mammography program, is used in the PBCT project. It is based on two custom-made high-precision ionization chambers placed approximately 3 m upstream from the sample (breast). The chambers measure the entrance radiation dose in terms of absolute air kerma which is used to define exposure parameters. Within a wide energy range (9–40 keV), the ionization chambers were calibrated against the standard air kerma chamber for low-energy X-rays by the Department of Ionizing Radiation Metrology of the Italian National Agency for New Technologies, Energy and Environment (ENEA) (Burns *et al.*, 1999; Bovi *et al.*, 2007, 2009). In a clinical scenario, the dosimetric system allows to measure the entrance radiation dose in real time throughout the examination. In case of any accidental event, potentially altering the predetermined level of radiation dose or compromising the image quality, the safety system is designed to promptly interrupt the examination by operating a fast shutter (closing time of 15 ms), thus ensuring patient's safety (Longo *et al.*, 2007).

The imaging device is a large-area high-efficiency direct-conversion photon-counting detector (Pixirad-8), based on a CdTe sensor bump-bonded on the readout ASIC (Bellazzini *et al.*, 2013). The readout electronics has been optimized to obtain a negligible dead-time between consecutive projection acquisitions, allowing to perform a continuous irradiation of the patient without losing counts or requiring shutter–detector synchronization. The detector is made up by eight modules, each one with an active area of 30.7 mm × 24.8 mm, leading to a global active area of 246 mm × 24.8 mm that fits well with the beam cross section. The pixels are arranged on a honeycomb matrix with a 60 µm pitch, corresponding to a matrix of 4096 × 476 pixels. Each pixel is associated with two independent 15-bit counters which can be used either in color mode or in dead-time-free mode. The first mode, which is suitable to polychromatic X-ray spectra applications, allows two different energy thresholds to be set, thus enabling spectral imaging (Brun *et al.*, 2018). When the latter mode is selected, as in the present study, both thresholds are set to the same value and one counter is filled while the other is being read, thus providing a virtually dead-time-free acquisition, with a linear response up to $2 \times 10^5$ counts pixel$^{-1}$ s$^{-1}$ (at 30 keV with 5 keV threshold). The maximum count rate detected during image acquisitions was of the order of $10^4$ counts pixel$^{-1}$ s$^{-1}$ (at 32 keV with 3 keV threshold), hence well within the linearity regime. Further details on the system's performances (*e.g.* spatial resolution, noise texture, operation modes) are reported by Delogu *et al.* (2016) and Vedantham *et al.* (2016). A comprehensive review of hybrid pixel detector architectures, including a thorough comparison of different sensors, can be found in Ballabriga *et al.* (2016).

### 2.2. Samples and acquisition parameters

The work reported in this paper was carried out following the Directive 2004/23/EC of the European Parliament and of the Council of 31 March 2004 on setting standards of quality and safety for the donation, procurement, testing, processing, preservation, storage and distribution of human tissues. The images presented in this study were acquired in order to guide the pathologist in the lesion localization during histological preparation, according to the standard procedures of the clinical operative unit (UCO) of the Anatomy and Histology Department of the University Hospital of Cattinara, Trieste. The samples were prepared from specimens of breast mastectomy and lumpectomy sent to the clinical operative unit. They were fixed in formalin and sealed in a vacuum bag. As reported in a previous work (Chen *et al.*, 2010), no substantial alterations in contrast between adipose and fibroglandular/tumoral tissue is expected at the selected energy due to the formalin fixation process. Three surgical specimens containing cancer were analyzed and characterized by expert pathologists:

(i) Sample A is a left simple mastectomy from a 86 year old woman. The histological exam revealed a high-grade infiltrating solid carcinoma with a maximum diameter of 8 cm.

(ii) Sample B is a lumpectomy in left upper inner breast from a 84 year old woman. The histological exam revealed a moderate-grade infiltrating ductal carcinoma with a maximum diameter of 2.4 cm with a central sclerotic area.

(iii) Sample C is a right simple mastectomy from a 77 year old woman. The histological exam revealed a moderate-grade infiltrating ductal carcinoma with a maximum diameter of 9 cm.

Thanks to the negligible divergence of the beam within the object (*i.e.* parallel beam geometry), the projections were collected only over 180°, thus speeding up the acquisition. The samples where imaged in continuous-rotation mode and the maximum available detector frame rate of 30 frames s$^{-1}$ was selected, corresponding to 1200 evenly spaced projections over 180°. Each scan was performed in 40 s with an angular speed of 4.5° s$^{-1}$. Given the small vertical dimension of the beam (3.5 mm), several scans (8 to 14) at different vertical table positions were needed to acquire the full volume, corresponding to a total scan time ranging from 5 to 9 min. All the specimens were imaged at 32 keV and the beam intensity

was adjusted by means of aluminium filters to deliver 5 mGy of total mean glandular dose.

### 2.3. Exposure and dose estimation

Total mean glandular dose ($MGD_t$) is the dosimetric quantity used to determine the desired photon fluence. $MGD_t$ is defined as the ratio between the total energy deposited in the whole breast and the glandular mass in the irradiated volume, as opposed to mean glandular dose (MGD), that is the mean dose to the glandular mass present in the whole breast (Mettivier *et al.*, 2016). It should be noted that, when irradiating only a portion of the breast, $MGD_t$ is a conservative dosimetric quantity since it accounts also for the energy scattered outside the irradiated volume. Moreover, as reported in Fig. 1, $MGD_t$ varies very slowly changing the thickness of irradiated region and it converges to MGD when the entire breast is irradiated. Thus, $MGD_t$ is an appropriate dosimetric quantity in a clinical scenario where only a partial scan of the breast is required (*e.g.* due to acquisition time constraints or previous knowledge of a specific region of interest). In practice, $MGD_t$ is calculated by multiplying the air kerma at breast position by a conversion factor accounting for breast size and glandularity, obtained from an *ad hoc* developed Monte Carlo simulation based on a *GEANT4* code optimized for breast dosimetry (Fedon *et al.*, 2015; Mettivier *et al.*, 2016). With the aim of establishing an easier way of comparison with results presented by other groups using different dosimetric protocols (Pacilè *et al.*, 2018; Baran *et al.*, 2017), the entrance air kerma is declared for each image in the results section.

### 2.4. Pre-processing, phase retrieval and reconstruction

Data processing of large-area high-$Z$ photon-counting detectors is, in most cases, challenging since the presence of multi-module architectures and the use of sensor materials which are difficult to produce with high purity (if compared with silicon) usually lead to detector-related artifacts in the acquired images (Mozzanica *et al.*, 2016; Delogu *et al.*, 2017*b*). In order to cope with these artifacts, the projection images undergo an *ad hoc* developed pre-processing procedure tailored on the Pixirad-8 detector characteristics. The procedure, which has been thoroughly discussed by Brombal *et al.* (2018*a*), consists of the following steps:

(i) Dynamic flat-field normalization, to correct pixel-to-pixel non-uniform response and time-dependent gain variations due to polarization/charge-trapping effects (Delogu *et al.*, 2017*a*).

(ii) Seaming, to fill the dead space between adjacent modules. This step is based on linear interpolation involving a kernel of 4 × 4 pixels next to the edge of each module.

(iii) Removal of speckles due to bad pixels by means of an alpha-trimmed filter.

(iv) Dynamic (*i.e.* projection index dependent) ring-removal procedure based on a rank filter and 3D Gaussian smoothing.

Once the raw data have been pre-processed, the phase-retrieval algorithm is applied to each projection. Phase retrieval can be seen as a bi-dimensional filter in the Fourier space $(u, v)$ which is written as

$$H(u, v) = \left[1 + \pi\lambda d \frac{\delta}{\beta}\left(u^2 + v^2\right)\right]^{-1}, \qquad (1)$$

where $\lambda$ is the radiation wavelength, $d$ is the propagation distance and $\delta/\beta$ is the ratio between the real and imaginary part of the refraction coefficient and, in Paganin's approach, it is assumed to be constant throughout the sample. A $\delta/\beta$ value of 2308, corresponding to (ICRU-44) breast tissue and extracted from a publicly available database (Taylor, 2015; White *et al.*, 2016), is used for all the samples. A comprehensive discussion on the phase-retrieval filter used for PBCT images, encompassing both a theoretical description and experimental results obtained by the SYRMA-CT/SYRMA-3D collaboration, has been given by Brombal *et al.* (2019) and Donato *et al.* (2019).

Following the application of the phase-retrieval algorithm, the images are reconstructed via a GPU-based FBP with a Shepp-Logan filtering (Brun *et al.*, 2015). It is worth noting that, due to the pixels' honeycomb geometry and the slight beam magnification, the reconstructed voxel size is 57 µm × 57 µm × 50 µm.

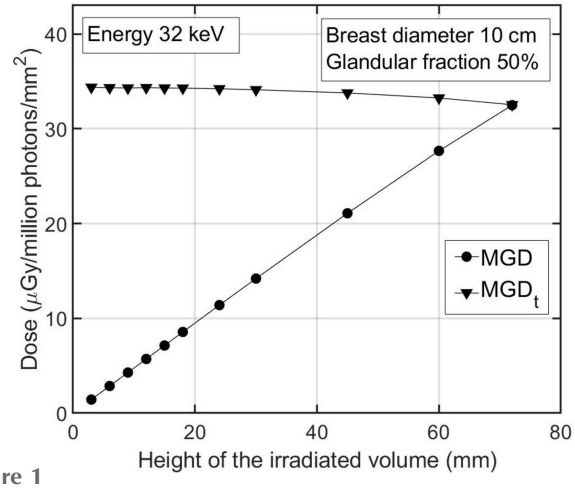


**Figure 1**
MGD (circles) and $MGD_t$ (triangles) as a function of the height of the irradiated volume, resulting from a Monte Carlo simulation of a cylindrical breast phantom (50% glandular fraction) with a diameter of 10 cm and a height of 7.5 cm, and a beam energy of 32 keV. MGD converges to $MGD_t$ upon irradiation of the whole phantom (Mettivier *et al.*, 2016).

## 3. Results

So far, most of the free-space propagation PBCT applications documented in the literature have been limited to scans of a single (or few) slice(s) of breast specimens (Pacilè *et al.*, 2015; Longo *et al.*, 2016; Baran *et al.*, 2017). It is clear that, to prove the advantages over conventional imaging, the three-dimensional potential of CT must be used by imaging the full volume as done, for instance, with other phase-sensitive techniques (Keyriläinen *et al.*, 2008; Zhao *et al.*, 2012; Brun *et al.*, 2014). In

recent publications, by both the Italian and Australian collaborations (Brombal *et al.*, 2018*b*; Pacilè *et al.*, 2018), the first full 3D reconstructions of breast specimens imaged with free-space propagation PBCT at clinically acceptable dose levels have been shown. In the following, based on full volume scans of three large mastectomy/lumpectomy samples, different aspects of PBCT images, including 3D visualization and convenient data processing, are presented. Moreover, in two cases, PBCT is compared with conventional X-ray pre-surgical imaging and, in one case, the matching between PBCT and histological images is demonstrated.

The reconstructed three-dimensional volume of the sample A is reported in Figs. 2(*a*)–2(*c*), displaying the three orthogonal view planes, *i.e.* sagittal, coronal and transverse (see inset). It should be noted that, to preserve the well established anatomical planes convention, the plane parallel to the beam, commonly referred to as transverse, is here defined as coronal. The sample has been scanned with an entrance air kerma of 8 mGy and its volume is approximately of 10 cm × 10 cm × 5 cm. From PBCT images the extension (maximum dimensions 5 cm × 5 cm × 5 cm) and morphology of the tumor can be evaluated. Remarkably, the multiple-plane view enabled by PBCT allows a clear evaluation of the various foci of the lesion, their connection as well as the skin involvement (see the arrows in figure). These kinds of features, which are often difficult or even impossible to evaluate using standard imaging techniques, are of major importance in the therapeutic management.

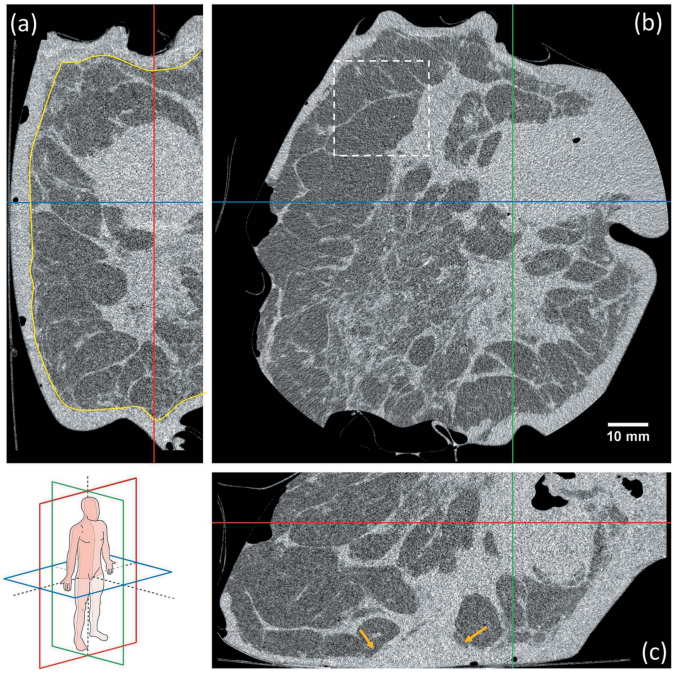


**Figure 2**
Sagittal (*a*), coronal (*b*), transverse (*c*) views of the sample A. Line markers are centered in the bulk of the biggest tumoral focus while several accumulations of desmoplastic tissue are visible throughout the breast volume. The curved yellow line in (*a*) indicates the skin margin, while the arrows in (*c*) indicate the skin involvement. The dashed square represents the crop region reported in Figs. 4(*a*)–4(*b*).

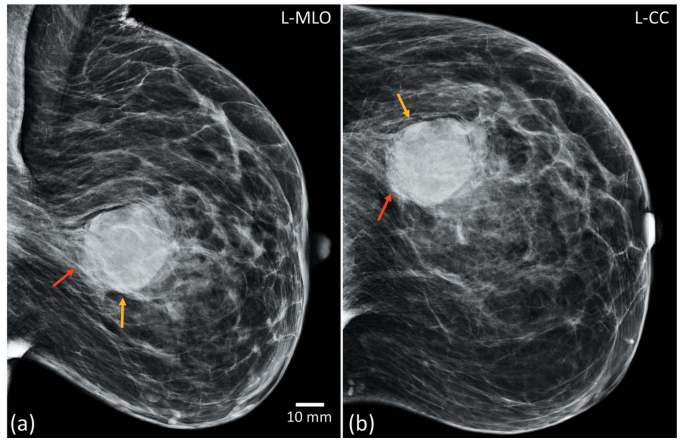


**Figure 3**
Mammographic images of the patient before surgery corresponding to sample A: medio-lateral view (*a*), cranio-caudal view (*b*). Sharp margins of the opacity are indicated by yellow arrows while shaded margins are indicated by red arrows.

For comparison, the mammographic scans acquired few weeks before surgery are reported in Figs. 3(*a*) and 3(*b*). The images show a high-density large round opacity (diameter of 4 cm) with some lobulations and, while part of its margins are observed to be sharp (yellow arrows), others are shaded and difficult to interpret (red arrows) due to tissue superposition. The opacity is surrounded by a non-homogeneous and non-specific less dense area. It is clear that in PBCT images the absence of tissues superposition allows a generally more accurate morphological description of the lesion, thus leading to a higher diagnostic confidence.

Of note, from the physical perspective, is the effect of phase retrieval on the visibility of fibroglandular details: Figs. 4(*a*) and 4(*b*) show a region of Fig. 2(*b*) containing a thin fibroglandular spicula, reconstructed without and with phase retrieval. Considering the respective line profiles of Figs. 4(*c*) and 4(*d*), the fibrous detail is clearly visible only when the phase retrieval is applied while, when the reconstruction is performed on non-phase-retrieved data, it is well below the noise level.

In Figs. 5(*a*)–5(*c*) three orthogonal views of the sample B, acquired with an entrance air kerma of 7 mGy, are shown. The scanned volume has dimensions of 9 cm × 8 cm × 4 cm, while the tumor bulk, identified by the crossing of line markers, is of 2.5 cm × 2.5 cm × 2 cm. Sharp interfaces between fibrous and adipose tissue and air gaps visible in the reconstruction are caused by surgical cuts performed during the formalin fixation. The tumor bulk embeds a hyper-dense sclerotic component [arrow in Fig. 5(*c*)] and several microcalcifications (red circles). The irregularity of the lesion margins, as well as their spiculated nature, are clearly visible, thus making the clinical picture compatible with a neoplastic lesion, as confirmed by histological examination. Moreover, focusing on the large calcification (diameter 1.4 mm) visible in the sample's periphery [upper part of Fig. 5(*a*)], it is interesting to observe the presence of a cavity in its center, typical of benign rim calcifications.

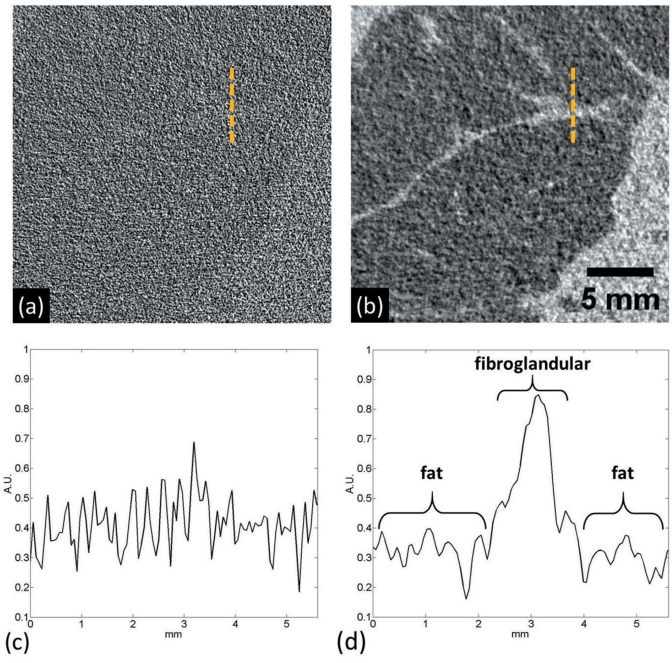


**Figure 4**
Detail reconstructed without (*a*) and with (*b*) phase retrieval. In (*c*) and (*d*) profiles along the dashed lines in (*a*) and (*b*), respectively, are reported.

In order to allow a direct comparison between PBCT and mammography, a slice oriented as the mammographic medio-lateral plane is chosen, using as a reference the large benign calcification located in the periphery of the sample, as marked by the arrows in Figs. 6(*a*)–6(*c*). It is clear that, while the

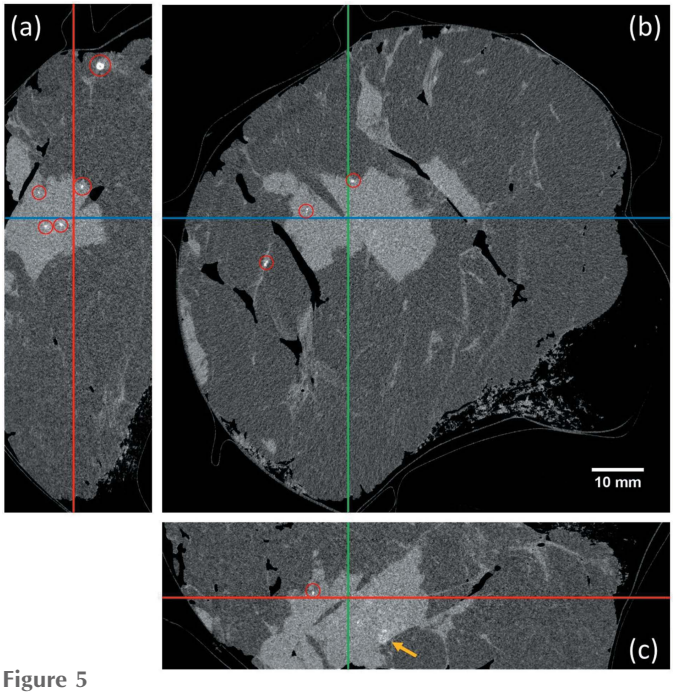


**Figure 5**
Sagittal (*a*), coronal (*b*), transverse (*c*) views of the sample B. Line markers are centered in the bulk of the lesion, while the arrow in (*c*) indicates the hyper-dense sclerotic component. Red circles indicate microcalcifications.

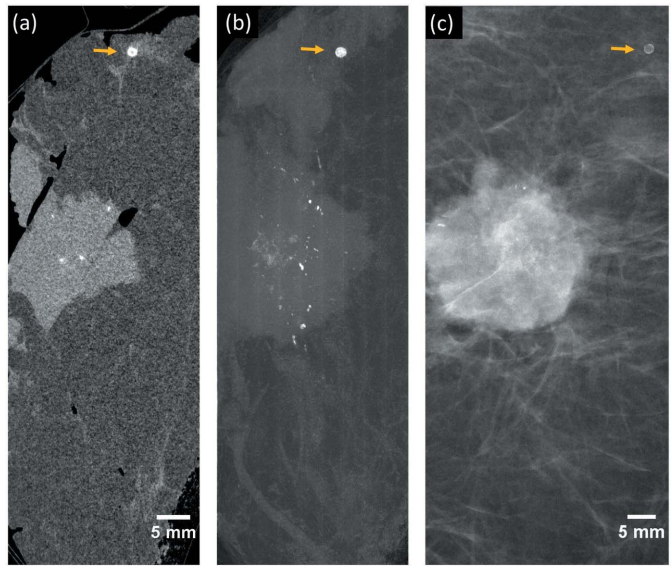


**Figure 6**
Single slice (*a*) and maximum intensity projection (*b*) of the sagittal view of sample B. A crop of the medio-lateral pre-surgery mammographic image is reported in (*c*). Arrows identify the benign rim calcification used as a reference.

mammographic image [Fig. 6(*c*)] represents an average of the absorption properties of a 4 cm-thick compressed breast, the 57 µm thickness of the CT slice [Fig. 6(*a*)] allows avoiding tissue superposition. Furthermore, thanks to the three-dimensional nature of PBCT data, several processing operations other than averaging can be performed and, if needed, condensed in bi-dimensional images which are more usual in breast imaging. As an example, in Fig. 6(*b*), the maximum intensity projection of the entire PBCT stack is reported. Remarkably, while a generally good match in lesion dimension and position is observed, tens of microcalcifications in the tumor region, missed by the mammographic examination, can be identified in one single maximum projection image.

In addition to orthogonal views display and bidimensional data reduction, PBCT images are suitable for 3D rendering as shown in Fig. 7. By adequately choosing the display thresholds, the fat tissue has been eliminated, fibroglandular/tumor structures have been made increasingly dark as a function of their density and the microcalcifications have been segmented (in red). A darker region can be seen within the tumor bulk enclosing several calcifications, that identify the hyper-dense sclerotic component of the lesion. In general, the main advantage of 3D rendering is the possibility of capturing, thanks to the depth perception, the global appearance of the lesion in terms of shape, distribution, extension and spiculation. Moreover, this kind of visualization is also suitable for further quantitative analysis, such as characterization of spatial and dimension distributions of microcalcifications, and modeling of the tumor. The effectiveness of 3D display is shown also in a video provided as supporting information.

Sample C is scanned with an entrance air kerma of 7 mGy and its dimensions are 10 cm × 10 cm × 3 cm. From the coronal view displayed in Fig. 8(*b*), the presence of a multi-

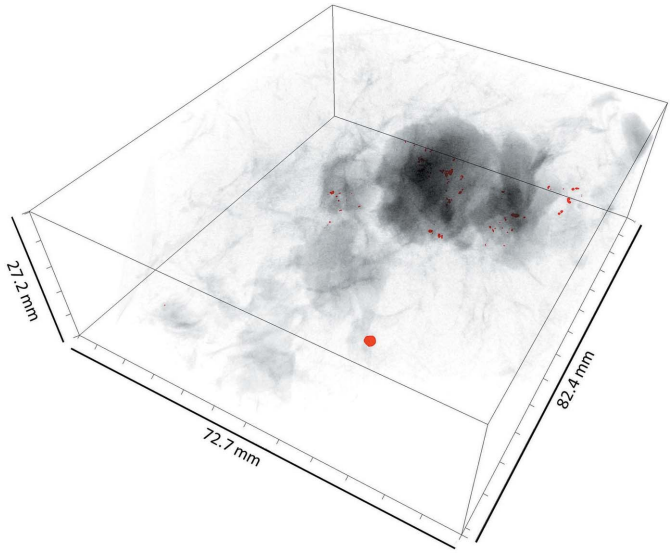


**Figure 7**
3D rendering of the sample B. Increasingly darker regions represent fibroglandular/tumoral tissue with increasing density, while red scattered volumes identify calcifications. The rendered volume is a sub-region of the whole scanned volume focusing on the lesion.

focal lesion, marked by the arrows in the image, can be observed. The line markers are centered on a portion of the lesion.

In Fig. 9 a zoomed detail with dimensions 2.5 cm × 2.5 cm obtained from the PBCT scan (*a*) is compared with the respective histological image (*b*). From the PBCT image a lesion with well defined smooth margins (black line) can be

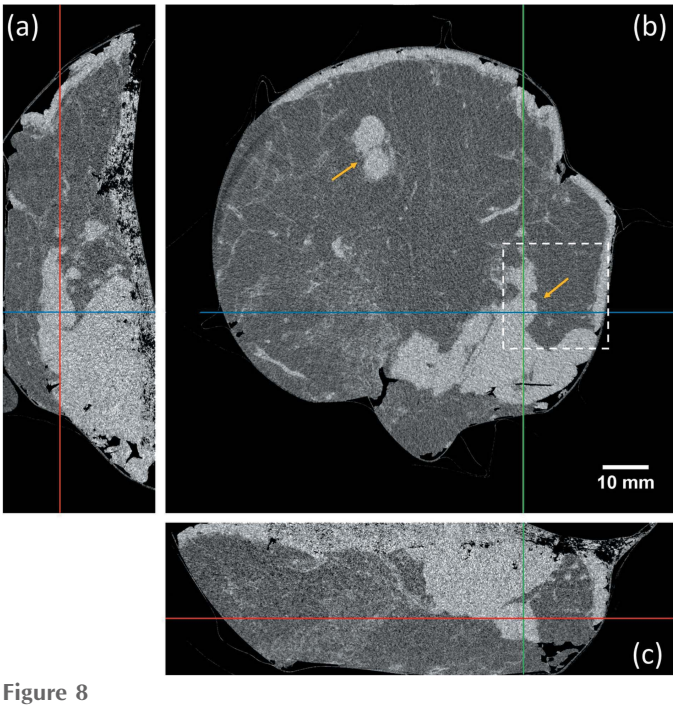


**Figure 8**
Sagittal (*a*), coronal (*b*), transverse (*c*) views of the sample C. Line markers are centered on one portion of the largest lesion, while arrows indicate two different tumor foci. Dashed line encloses the detail shown in Fig. 9.

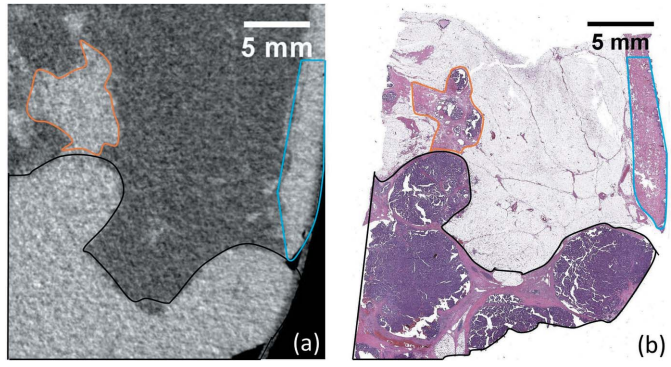


**Figure 9**
Comparison between PBCT (*a*) and histology (*b*). In both images, the region enclosed by the black line is an encapsulated lesion, the one within the orange line encloses ductal structures with papillary lesion, the one within the light blue line is skin.

clearly distinguished from a contiguous structure with irregular margins (orange line). The distinction of the two structures is confirmed by matching the tomographic image with the histological examination, showing an encapsulated tumor (black line) and separated ductal structures with papillary lesion (orange line). The light blue line identifies a thickened skin tissue portion which has similar shape and orientation in both PBCT and histological images.

It should be remarked that the possibility of matching radiological and histological images (with low radiation dose) is peculiar of the proposed PBCT system. In fact, both mammography and tomosynthesis imaging suffer from tissue superposition effects whereas other 3D techniques (*e.g.* MRI) have, in general, an insufficient spatial resolution.

### 3.1. Future developments

Improving any X-ray based radiological technique means either increasing details' visibility at a constant radiation dose or, equivalently, preserving a given visibility with a lower delivered dose. In this context, for PBCT images, the propagation distance plays a crucial role in terms of image quality. In particular, Nesterets and Gureyev have demonstrated that, given the validity of the transport of intensity, the signal-to-noise ratio (SNR) gain due to phase retrieval increases (as a first approximation) linearly with the propagation distance without altering image contrast and spatial resolution (Nesterets & Gureyev, 2014; Gureyev *et al.*, 2017). This theoretical framework is supported by recently published studies based on lung and breast tissues (Kitchen *et al.*, 2017; Brombal *et al.*, 2018*c*). In particular, the results by Brombal *et al.* (2018*c*), reported in Fig. 10, are based on the same experimental setup and on specimens of comparable size and composition with respect to the ones presented in this study. Following the red curve in the top panel, it can be seen that the SNR doubles moving from 1.6 m, corresponding to the actual patient-to-detector distance, to 3.5 m of propagation distance, while it is approximatively four times higher at 6 m. This SNR increase is obtained at constant spatial resolution (central panel) and contrast (bottom panel), with a fixed detector

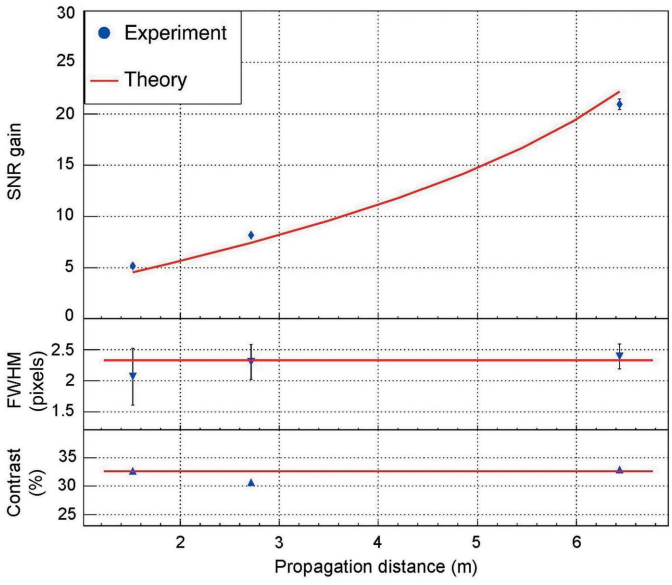


**Figure 10**
Comparison between experimental results (blue points) and theoretical predictions (red lines) of the model reported by Nesterets & Gureyev (2014) as a function of the propagation distance. Adapted with permission from Brombal *et al.* (2018*c*).

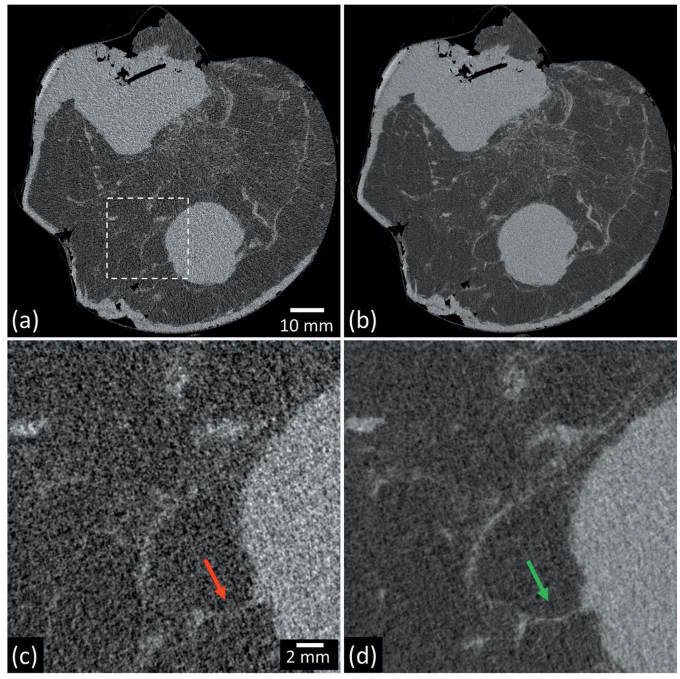


**Figure 11**
Scan of the sample C acquired at $MGD_t$ of 5 mGy and SNR = 9.1 (*a*), 20 mGy and SNR = 18.8 (*b*), mimicking a 5 mGy acquisition at the upgraded SYRMEP beamline. In (*c*) and (*d*) a zoom of a detail of (*a*) and (*b*), as shown by the dashed line, is reported. The arrows point toward a fibroglandular spicula which is not visible in (*c*) (red) and visible in (*d*) (green). SNR is measured within the spheroidal hyperdense mass.

fluence. In light of these results, the SYRMEP beamline is being redesigned to accommodate propagation distances up to 4 m (the longest distance available) by moving the detector downstream with respect to the patient support position (that is fixed). This upgrade is expected to improve the SNR by approximately a factor of two, even when both the small changes in magnification due to larger distance (from 1.05 at 1.6 m to 1.13 at 4 m) and the flux reduction (about 10% at 32 keV) due to the increased air attenuation are taken into account.

In order to give an idea of the expected image quality improvement after the upgrade, images with a two-fold higher SNR (*i.e.* four-fold higher dose, 20 mGy $MGD_t$) have been acquired and compared with the present 5 mGy reference, as shown in Fig. 11(*a*)–11(*b*). By zooming on a detail enclosing the margins of the main lesion [panels (*c*)–(*d*)], it is clear that increasing the SNR by a factor of two allows to determine the presence of a connection between the lesion and a fibroglandular spicula (green arrow), which is missed in the reference image (red arrow). Of note, the actual impact of the beamline upgrade will be assessed through dedicated measurements.

Along with the optimization of physical parameters, such as energy and propagation distance, a lot of effort is being dedicated to *ad hoc* reconstruction algorithms. Albeit the presented images are reconstructed using standard FBP, some promising results obtained by using iterative algorithms have been reported (Donato *et al.*, 2019). In particular, the use of a dedicated SART algorithm (Kak *et al.*, 2002), combined with a 3D bilateral filter used as a regularization filter during the iterative process (Golosio *et al.*, 2004; Oliva *et al.*, 2017), has proven to be a valid alternative to FBP, allowing a significant improvement in terms of SNR. This is qualitatively shown in Fig. 12, displaying a section of sample C reconstructed with FBP (*a*) and SART (*b*) at 5 mGy of dose level. The application of SART results in a 40% improvement in SNR (measured within the spheroidal lesion), while no evident degradation in terms of spatial resolution is observed, as visible in the detail in panels (*c*)–(*d*). An extensive study aiming to optimize and compare several reconstruction algorithms is now underway and will be presented in a separate paper.

## 4. Discussion and conclusions

This work represents a leap forward in the clinical implementation of phase-contrast breast CT at Elettra. Three-dimensional images of three large breast specimens have been acquired with the updated experimental setup, encompassing a detector upgrade and dedicated pre-processing procedure, continuous rotation acquisition and an *ad hoc* dosimetric system. PBCT images have been compared with standard mammographic images, demonstrating that the high spatial and contrast resolution, combined with the 3D nature of tomographic data which allows to avoid tissue superposition, determines a more accurate morphological description of neoplastic lesions. The detailed characterization of a lesion in terms of its volume, shape, margins, number and morphology of calcifications, can lead to clinically relevant conclusions on its malign/benign nature, invasiveness and grading.

It should be remarked that issues such as detection of microcalcifications and reduction of tissue superposition are

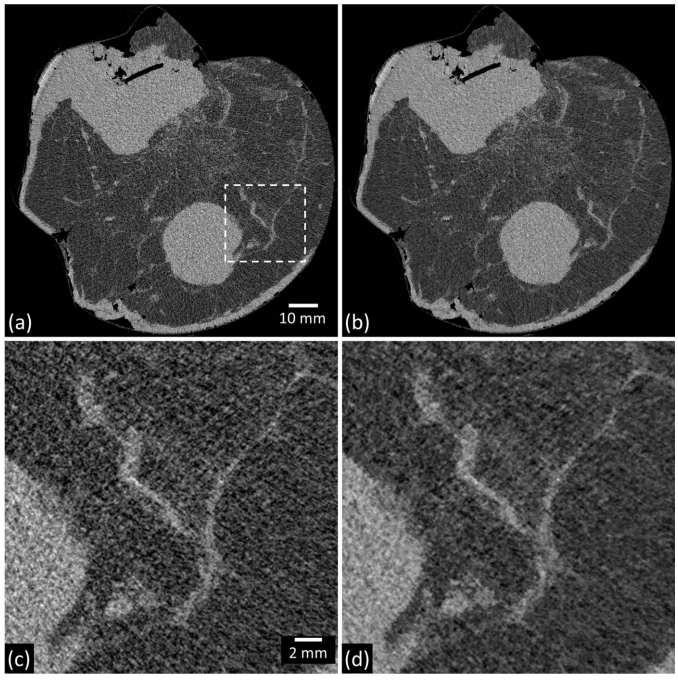


**Figure 12**
Scan of the sample C reconstructed via FPB (*a*) and *ad hoc* SART (*b*) algorithms. In (*c*) and (*d*) a zoomed detail of (*a*) and (*b*), as indicated by the dashed line, is shown. SNR measured within the spheroidal mass is 9.1 in (*a*) and 12.8 in (*b*).

now being investigated also by digital breast tomosynthesis (DBT) (Sechopoulos, 2013). DBT is an emerging technology that provides a pseudo-3D reconstruction of the breast by acquiring multiple projections over a limited angular span. Several clinical trials are currently underway to better understand its role in breast cancer screening and diagnosis and, at present, there are mixed reports regarding DBT capabilities in microcalcification detection (Marinovich *et al.*, 2018; Choi *et al.*, 2019). In addition, it should be stressed that, while BCT is a fully three dimensional technique, DBT images contain pseudo-3D information, *e.g.* not allowing operations such as re-slicing in other view planes.

Conversely, the possibility offered by PBCT of processing fully three-dimensional data, concentrating some features in bi-dimensional images, may be appealing to radiologist mostly familiar with planar or quasi-planar mammographic techniques. As reported in the study, the application of maximum intensity operations could be of use to highlight the presence of calcifications in a single image, with a higher sensitivity if compared with conventional radiology. The availability of high-resolution tomographic datasets paves the way for 3D rendering and segmentation of the acquired images, which could be a valuable tool for evaluating the spatial distribution of lesions and microcalcifications, serving as a reference to the surgeon in the pre-surgery planning. Given the good matching observed between PBCT and histological images even at low (*i.e.* clinically acceptable) delivered dose, the use of PBCT in a clinical scenario opens up the possibility of performing a more accurate tumor grading (TNM classification), where a precise assessment of lesion dimension is crucial, and it can serve as a guide in the specimen cutting process during pathological examination.

Furthermore, a major improvement in the visibility of soft tissue details is expected thanks to the upgrade of the SYRMEP beamline which is now underway, allowing to use longer propagation distances (up to 4 m). The final goal is to increase the SNR of tomographic images at a constant radiation dose by a factor of two or, equivalently, to preserve the same image quality with a dose reduction by a factor of four. At the same time, *ad hoc* iterative techniques, aiming for a further improvement of SNR with respect to the conventional FBP approach, are being developed.

In sight of the clinical implementation, one of the main concerns is the exam duration, which should be as short as possible to ensure patient comfort and to reduce artifacts related to voluntary movement. In this context, the implementation of an *ad hoc* shaped filter to flatten the vertical beam profile would allow to use a wider vertical portion of the beam (from 3.5 mm to $\gtrsim$5 mm), thus reducing the total scan time by a 30% or more. At the same time, the reduction of the number of projections along with the use of iterative techniques, as recently reported by Donato *et al.* (2019), would allow a reduction of a further 20 to 30% in the scan time still retaining a comparable image quality. The combined effect of these improvements will be a reduction of about 50% in the overall exam duration.

## Acknowledgements

The SYRMA-3D project is supported by Istituto Nazionale di Fisica Nucleare (National Scientific Committee 5 for Technological and Inter-disciplinary Research) and Elettra-Sincrotrone Trieste SCpA. SD is partially supported by Consorzio per la Fisica Trieste.

## References

AB-CT (2019). *Advanced Breast-CT*, https://www.ab-ct.com/nuview/.
Ballabriga, R., Alozy, J., Campbell, M., Frojdh, E., Heijne, E., Koenig, T., Llopart, X., Marchal, J., Pennicard, D., Poikela, T., Tlustos, L., Valerio, P., Wong, W. & Zuber, M. (2016). *J. Instrum.* **11**, P01007.
Baran, P., Pacile, S., Nesterets, Y., Mayo, S., Dullin, C., Dreossi, D., Arfelli, F., Thompson, D., Lockie, D., McCormack, M., Taba, S. T., Brun, F., Pinamonti, M., Nickson, C., Hall, C., Dimmock, M., Zanconati, F., Cholewa, M., Quiney, H., Brennan, P. C., Tromba, G. & Gureyev, T. E. (2017). *Phys. Med. Biol.* **62**, 2315–2332.
Bellazzini, R., Spandre, G., Brez, A., Minuti, M., Pinchera, M. & Mozzo, P. (2013). *J. Instrum.* **8**, C02028.
Berger, N., Marcon, M., Saltybaeva, N., Kalender, W. A., Alkadhi, H., Frauenfelder, T. & Boss, A. (2019). *Invest. Radiol.* doi:10.1097/RLI.0000000000000552.
Bovi, M., Laitano, R., Pimpinella, M., Toni, M., Casarin, K., Quail, E., Tromba, G., Vacotto, A. & Dreossi, D. (2007). *Workshop on Absorbed Dose and Air Kerma Primary Standards*, Paris, France.
Bovi, M., Laitano, R., Pimpinella, M., Toni, M., Casarin, K., Tromba, G. & Vascotto, A. (2009). *Proceedings of the 6th Conference Metrologia & Qualità*, Turin, Italy, pp. 7–9.
Brombal, L., Donato, S., Brun, F., Delogu, P., Fanti, V., Oliva, P., Rigon, L., Di Trapani, V., Longo, R. & Golosio, B. (2018*a*). *J. Synchrotron Rad.* **25**, 1068–1077.
Brombal, L., Donato, S., Dreossi, D., Arfelli, F., Bonazza, D., Contillo, A., Delogu, P., Di Trapani, V., Golosio, B., Mettivier, G., Oliva, P.,

Rigon, L., Taibi, A. & Longo, R. (2018*c*). *Phys. Med. Biol.* **63**, 24NT03.
Brombal, L., Golosio, B., Arfelli, F., Bonazza, D., Contillo, A., Delogu, P., Donato, S., Mettivier, G., Oliva, P., Rigon, L., Taibi, A., Tromba, G., Zanconati, F. & Longo, R. (2018*b*). *Proc. SPIE*, **10573**, 1057320.
Brombal, L., Golosio, B., Arfelli, F., Bonazza, D., Contillo, A., Delogu, P., Donato, S., Mettivier, G., Oliva, P., Rigon, L., Taibi, A., Tromba, G., Zanconati, F. & Longo, R. (2019). *J. Med. Imaging*, **6**, 031402.
Brun, E., Grandl, S., Sztrókay-Gaul, A., Barbone, G., Mittone, A., Gasilov, S., Bravin, A. & Coan, P. (2014). *Med. Phys.* **41**, 111902.
Brun, F., Di Trapani, V., Dreossi, D., Rigon, L., Longo, R. & Delogu, P. (2018). *IFMBE Proc.* **61**, 123–126.
Brun, F., Pacilè, S., Accardo, A., Kourousias, G., Dreossi, D., Mancini, L., Tromba, G. & Pugliese, R. (2015). *Fund. Inform.* **141**, 233–243.
Burns, D., Toni, M. & Bovi, M. (1999). *Comparison of the air-kerma standards of the ENEA-INMRI and the BIPM in the low-energy X-ray range.* Technical Report BIPM-99/11. Bureau International des Poids et Mesures.
Castelli, E., Tonutti, M., Arfelli, F., Longo, R., Quaia, E., Rigon, L., Sanabor, D., Zanconati, F., Dreossi, D., Abrami, A., Quai, E., Bregant, P., Casarin, K., Chenda, V., Menk, R. H., Rokvic, T., Vascotto, A., Tromba, G. & Cova, M. A. (2011). *Radiology*, **259**, 684–694.
Chen, R., Longo, R., Rigon, L., Zanconati, F., De Pellegrin, A., Arfelli, F., Dreossi, D., Menk, R., Vallazza, E., Xiao, T. & Castelli, E. (2010). *Phys. Med. Biol.* **55**, 4993–5005.
Choi, J. S., Han, B.-K., Ko, E. Y., Kim, G. R., Ko, E. S. & Park, K. W. (2019). *Eur. Radiol.* **29**, 319–329.
Cloetens, P., Barrett, R., Baruchel, J., Guigay, J.-P. & Schlenker, M. (1996). *J. Phys. D Appl. Phys.* **29**, 133–146.
Coan, P., Bravin, A. & Tromba, G. (2013). *J. Phys. D Appl. Phys.* **46**, 494007.
Contillo, A., Veronese, A., Brombal, L., Donato, S., Rigon, L., Taibi, A., Tromba, G., Longo, R. & Arfelli, F. (2018). *Radiol. Oncol.* **52**, 329–336.
Delogu, P., Brombal, L., Trapani, V. D., Donato, S., Bottigli, U., Dreossi, D., Golosio, B., Oliva, P., Rigon, L. & Longo, R. (2017*b*). *J. Instrum.* **12**, C11014.
Delogu, P., Golosio, B., Fedon, C., Arfelli, F., Bellazzini, R., Brez, A., Brun, F., Lillo, F. D., Dreossi, D., Mettivier, G., Minuti, M., Oliva, P., Pichera, M., Rigon, L., Russo, P., Sarno, A., Spandre, G., Tromba, G. & Longo, R. (2017*a*). *J. Instrum.* **12**, C01016.
Delogu, P., Oliva, P., Bellazzini, R., Brez, A., de Ruvo, P., Minuti, M., Pinchera, M., Spandre, G. & Vincenzi, A. (2016). *J. Instrum.* **11**, P01015.
Donato, S., Brombal, L., Tromba, G., Longo, R., *et al.* (2019). *IFMBE Proc.* **61**, 109–115.
Fedon, C., Longo, F., Mettivier, G. & Longo, R. (2015). *Phys. Med. Biol.* **60**, N311–N323.
Fedon, C., Rigon, L., Arfelli, F., Dreossi, D., Quai, E., Tonutti, M., Tromba, G., Cova, M. A. & Longo, R. (2018). *J. Med. Imaging*, **5**, 013503.
Golosio, B., Brunetti, A. & Cesareo, R. (2004). *Nucl. Instrum. Methods Phys. Res. B*, **213**, 108–111.
Gureyev, T. E., Nesterets, Y. I., Kozlov, A., Paganin, D. M. & Quiney, H. M. (2017). *J. Opt. Soc. Am. A*, **34**, 2251–2260.
Kak, A. C., Slaney, M. & Wang, G. (2002). *Med. Phys.* **29**, 107.
Kalender, W. A., Beister, M., Boone, J. M., Kolditz, D., Vollmar, S. V. & Weigel, M. C. (2012). *Eur. Radiol.* **22**, 1–8.
Kalender, W. A., Kolditz, D., Steiding, C., Ruth, V., Luck, F., Roler, A.-C. & Wenkel, E. (2017). *Eur. Radiol.* **27**, 1081–1086.
Keyriläinen, J., Fernández, M., Karjalainen-Lindsberg, M.-L., Virkkunen, P., Leidenius, M., von Smitten, K., Sipilä, P., Fiedler, S., Suhonen, H., Suortti, P. & Bravin, A. (2008). *Radiology*, **249**, 321–327.
Kitchen, M. J., Buckley, G. A., Gureyev, T. E., Wallace, M. J., Andres-Thio, N., Uesugi, K., Yagi, N. & Hooper, S. B. (2017). *Sci. Rep.* **7**, 15953.
Koning, C. (2018). *Koning Breast CT*, http://koninghealth.com/en/kbct/.
Lindfors, K. K., Boone, J. M., Nelson, T. R., Yang, K., Kwan, A. L. & Miller, D. F. (2008). *Radiology*, **246**, 725–733.
Longo, R. (2016). *Nucl. Instrum. Methods Phys. Res. A*, **809**, 13–22.
Longo, R., Abrami, A., Arfelli, F., Bregant, P., Chenda, V., Cova, M. A., Dreossi, D., De Guarrini, F., Menk, R., Quai, E., Rokvic, T., Tonutti, M., Tromba, G., Zanconati, F. & Castelli, E. (2007). *Proc. SPIE*, **6510**, 65100T.
Longo, R., Arfelli, F., Bellazzini, R., Bottigli, U., Brez, A., Brun, F., Brunetti, A., Delogu, P., Di Lillo, F., Dreossi, D., Fanti, V., Fedon, C., Golosio, B., Lanconelli, N., Mettivier, G., Minuti, M., Oliva, P., Pinchera, M., Rigon, L., Russo, P., Sarno, A., Spandre, G., Tromba, G. & Zanconati, F. (2016). *Phys. Med. Biol.* **61**, 1634–1649.
Longo, R., Tonutti, M., Rigon, L., Arfelli, F., Dreossi, D., Quai, E., Zanconati, F., Castelli, E., Tromba, G. & Cova, M. A. (2014). *Philos. Trans. R. Soc. A*, **372**, 20130025.
Marinovich, M. L., Hunter, K. E., Macaskill, P. & Houssami, N. (2018). *J. Natl Cancer Inst.* **110**, 942–949.
Mettivier, G., Fedon, C., Di Lillo, F., Longo, R., Sarno, A., Tromba, G. & Russo, P. (2016). *Phys. Med. Biol.* **61**, 569–587.
Mittone, A., Bravin, A. & Coan, P. (2014). *Phys. Med. Biol.* **59**, 2199–2217.
Morita, T., Yamada, M., Kano, A., Nagatsuka, S., Honda, C. & Endo, T. (2008). *International Workshop on Digital Mammography, Lecture Notes in Computer Science*, Vol. 5116, pp. 48–54. Springer.
Mozzanica, A., Bergamaschi, A., Brueckner, M., Cartier, S., Dinapoli, R., Greiffenberg, D., Jungmann-Smith, J., Maliakal, D., Mezza, D., Ramilli, M., Ruder, C., Schaedler, L., Schmitt, B., Shi, X. & Tinti, G. (2016). *J. Instrum.* **11**, C02047.
Nesterets, Y. I. & Gureyev, T. E. (2014). *J. Phys. D Appl. Phys.* **47**, 105402.
O'Connell, A., Conover, D. L., Zhang, Y., Seifert, P., Logan-Young, W., Lin, C. L., Sahler, L. & Ning, R. (2010). *Am. J. Roentgenol.* **195**, 496–509.
O'Connell, A. M., Karellas, A. & Vedantham, S. (2014). *Breast J.* **20**, 592–605.
Oliva, P., Golosio, B., Arfelli, F., Delogu, P., Di Lillo, F., Dreossi, D., Fanti, V., Fardin, L., Fedon, C., Mettivier, G., *et al.* (2017). *2017 IEEE Nuclear Science Symposium and Medical Imaging Conference (NSS/MIC)*, 21–28 October 2017, Atlanta, GA, USA. IEEE.
Pacilè, S., Baran, P., Dullin, C., Dimmock, M., Lockie, D., Missbach-Guntner, J., Quiney, H., McCormack, M., Mayo, S., Thompson, D., Nesterets, Y., Hall, C., Pavlov, K., Prodanovic, Z., Tonutti, M., Accardo, A., Fox, J., Tavakoli Taba, S., Lewis, S., Brennan, P., Hausermann, D., Tromba, G. & Gureyev, T. (2018). *J. Synchrotron Rad.* **25**, 1460–1466.
Pacilè, S., Brun, F., Dullin, C., Nesterets, Y., Dreossi, D., Mohammadi, S., Tonutti, M., Stacul, F., Lockie, D., Zanconati, F., Accardo, A., Tromba, G. & Gureyev, T. E. (2015). *Biomed. Opt. Expr.* **6**, 3099–3112.
Paganin, D., Mayo, S., Gureyev, T. E., Miller, P. R. & Wilkins, S. W. (2002). *J. Microsc.* **206**, 33–40.
Rigon, L. (2014). *Compr. Biomed. Phys.* **2**, 193–216.
Rößler, A., Wenkel, E., Althoff, F. & Kalender, W. (2015). *Senologie Z. Mammadiagn. Ther.* **12**, 96–103.
Sarno, A., Mettivier, G., Golosio, B., Oliva, P., Spandre, G., Di Lillo, F., Fedon, C., Longo, R. & Russo, P. (2016). *Phys. Med.* **32**, 681–690.
Sarno, A., Mettivier, G. & Russo, P. (2015). *Med. Phys.* **42**, 2786–2804.
Sechopoulos, I. (2012). *Med. Phys.* **39**, 2896–2903.
Sechopoulos, I. (2013). *Med. Phys.* **40**, 014301.

Tanaka, T., Honda, C., Matsuo, S., Noma, K., Oohara, H., Nitta, N., Ota, S., Tsuchiya, K., Sakashita, Y., Yamada, A., Yamasaki, M., Furukawa, A., Takahashi, M. & Murata, K. (2005). *Invest. Radiol.* **40**, 385–396.

Taylor, J. A. (2015). *CSIRO TS imaging*, http://ts-imaging.science.unimelb.edu.au/Services/Simple/ICUtilXdata.aspx.

Tromba, G., Longo, R., Abrami, A., Arfelli, F., Astolfo, A., Bregant, P., Brun, F., Casarin, K., Chenda, V., Dreossi, D., Hola, M., Kaiser, J., Mancini, L., Menk, R. H., Quai, E., Quaia, E., Rigon, L., Rokvic, T., Sodini, N., Sanabor, D., Schultke, E., Tonutti, M., Vascotto, A., Zanconati, F., Cova, M., Castelli, E. & Siu, K. K. W. (2010). *AIP Conf. Proc.* **1266**, 18–23.

Vedantham, S., Shrestha, S., Karellas, A., Shi, L., Gounis, M. J., Bellazzini, R., Spandre, G., Brez, A. & Minuti, M. (2016). *Med. Phys.* **43**, 2118–2130.

Vincenzi, A., de Ruvo, P., Delogu, P., Bellazzini, R., Brez, A., Minuti, M., Pinchera, M. & Spandre, G. (2015). *J. Instrum.* **10**, C04010.

White, D. R., Wilson, I. J., Booz, J., Spokas, J. J. & Griffith, R. V. (2016). *J. Intl Commission Radiat. Units Measurements*, **os23**, NP.

Wienbeck, S., Lotz, J. & Fischer, U. (2017). *Clin. Imaging*, **42**, 50–59.

Zhao, Y., Brun, E., Coan, P., Huang, Z., Sztrókay, A., Diemoz, P. C., Liebhardt, S., Mittone, A., Gasilov, S., Miao, J. & Bravin, A. (2012). *Proc. Natl Acad. Sci.* **109**, 18290–18294.